

Ingress of Li into Solid Electrolytes: Cracking and Sparsely Filled Cracks

Dipayan Mukherjee, Shuai Hao, Paul R. Shearing, Robert M. McMeeking, Norman A. Fleck, and Vikram S. Deshpande*

The growth of Li dendrites in a solid electrolyte is commonly idealized by a pressure-filled crack. Recent observations in both garnet and sulfide electrolytes show that sparsely filled cracks exist prior to shorting of the cell, thereby invalidating this assumption. Herein, a variational principle that uses the Onsager formalism to couple Li deposition into the crack, elastic deformation of the electrolyte, and cracking of the electrolyte with the electrochemical driving forces and dissipation within the electrolyte and interfaces is developed. Consistent with observations, it is shown that Li ingress and cracking occur together for garnet electrolytes, but the cracks are sparsely filled. This sparse filling is a direct consequence of the mismatch between the elastic opening of the cracks and the deposition of Li into the cracks across the crack flanks. An increase in the resistance of Li ingress into the tips of Li filaments results in crack propagating ahead of the Li filaments, as observed for sulfide electrolytes. In such cases, the cracks are largely dry. The results provide a framework to model Li ingress into solid electrolytes and explain why the observations are qualitatively so different from dendrites in liquid electrolytes.

filament/dendrite penetration from the Li metal anode when the current density of the anode exceeds a critical current density (CCD).^[1,4–6] It is desirable to enhance the CCD of a SSB in order to allow for faster charging of electric vehicles, for example.

Several factors influence the CCD. For example, the CCD decreases with increasing grain size of the ceramic electrolyte^[7–9] and also decreases with increasing electrolyte/electrode interface ionic resistance.^[9–12] Recent observations^[13–16] suggest that dendrites grow in the vicinity of voids in Li anodes at the electrode/electrolyte interface. These voids form during the stripping phase, and the required current to grow these voids is typically much less than the CCD for dendrite propagation. These observations of void formation in the metal electrode and associated Li metal penetration are very general and qualitatively similar observations have also been reported for Na⁺/beta-alumina systems.^[17]


The assessment of dendrite propagation in ceramic electrolytes has, to-date, been restricted to modeling them as pressurized cracks.^[5,18–22] This concept was first used to explain dendrite formation in Na⁺/beta-alumina systems^[23] and has been extended more recently to Li dendrite formation in garnet electrolytes.^[5,18,20] While details of the models differ, all assume that the Na or Li have a sufficiently low shear strength that they behave as a fluid, and consequently crack propagation is driven

1. Introduction

Solid-state batteries (SSBs) with lithium (Li) metal anodes offer the possibility of enhanced energy density and enhanced safety. These SSBs typically employ ceramic electrolytes such as the Li-stuffed garnet Li₇La₃Zr₂O₁₂ (LLZO) or sulfides such as argyrodite (Li₆PS₅Cl) or LPS (Li₂S – P₂S₅).^[1–3] However, fully dense ceramic electrolytes can suffer from short circuits due to Li

D. Mukherjee, N. A. Fleck, V. S. Deshpande
Department of Engineering
University of Cambridge
Cambridge CB2 1PZ, UK
E-mail: vsd@eng.cam.ac.uk

S. Hao, P. R. Shearing
Electrochemical Innovation Lab
Department of Chemical Engineering
University College London
London WC1E 7JE, UK

 The ORCID identification number(s) for the author(s) of this article can be found under <https://doi.org/10.1002/ssstr.202300022>.

© 2023 The Authors. Small Structures published by Wiley-VCH GmbH. This is an open access article under the terms of the Creative Commons Attribution License, which permits use, distribution and reproduction in any medium, provided the original work is properly cited.

DOI: 10.1002/ssstr.202300022

S. Hao
Institute of New Energy Material Chemistry
School of Materials Science and Engineering
Nankai University
Tianjin 300021, China

P. R. Shearing, N. A. Fleck, V. S. Deshpande
The Faraday Institution
Quad One, Harwell Science and Innovation Campus
Didcot, UK

R. M. McMeeking
Department of Mechanical Engineering & Materials Department
University of California
Santa Barbara, CA 93106, USA

by the high fluid pressure generated by the electric overpotential across the crack flanks.^[21,24,25] In a slightly different vein, Shishvan et al.^[26,27] assumed that dendrites possess the same geometry as parallel sided-edge dislocations, with penetrating Li metal forming the “extra half-plane” of the edge dislocation. A defining feature of all these models is that the crack advance and Li/Na metal deposition within the crack proceed in unison: the metal completely fills the crack and the plating out of metal at the crack tip drives crack propagation.

The idealization of a dendrite as a pressurized crack or a macrodislocation is called into question by recent X-ray computed tomographic (X-ray CT) observations and associated measurements. Bruce and co-workers^[28] reported X-ray CT observations which clearly show that cracks propagate in Argyrodite-type LPS ($\text{Li}_6\text{PS}_5\text{Cl}$) electrolytes as empty, dry cracks: Li metal is only present at the crack mouth near the plating electrode. They reported that a through-crack develops after 25 min in an electrolyte of thickness 1 mm when the imposed current is $i_\infty = 1.5 \text{ mA cm}^{-2}$, but the cell does not immediately short. This was subsequently confirmed for LPS electrolytes by the X-ray CT observations of Shearing et al.^[29] reproduced in **Figure 1a**: the electrolyte cracked through its thickness, but Li (shaded in red) is present only near the plating electrode. In fact, at the time of through-cracking of the electrolyte, only about 20%

of the volume of the crack is occupied by Li. In contrast, for the case of an LLZO electrolyte, through-cracking and shorting occur almost simultaneously (and at a shorting time on the order for 2–10 mins which is much less than that for LPS^[10]). This suggests that the above-described pressurized crack models are applicable for LLZO. However, using nano-X-ray CT methods Shearing et al.^[30] observed that, while Li penetration and cracking occur approximately in unison for LLZO, the cracks within LLZO are only sparsely filled (Figure 1b). Collectively, these observations suggest that there remains a lack of understanding of the mechanisms by which dendrites propagate into solid electrolytes; current modeling frameworks are not reconciled with experimental observations.

All models to date employ a quasi-equilibrium approximation which governs the pressure/state of the Li within the crack. This assumption inherently results in the pressurized and filled crack prediction which seems inconsistent with observations. Here we shall use the Onsager formalism to develop a nonequilibrium, kinetic framework for the penetration of Li into ceramic electrolytes. The shape, filling, and propagation of the crack by Li filaments/deposits are natural outcomes of the solution of the variational principle. We shall show that, unlike in liquid electrolytes where elasticity of the electrolyte plays no role, sparsely filled cracks are to be expected due to the mismatch between

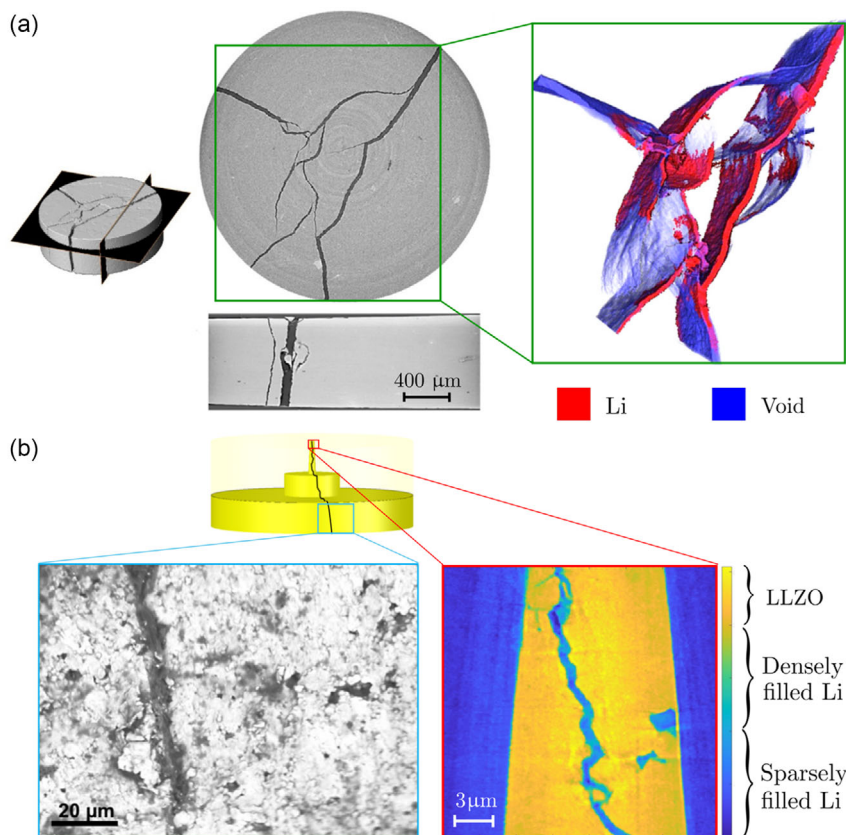


Figure 1. a) Optical micrograph and corresponding X-ray CT reconstruction of the crack in LPS showing that while the electrolyte has completely cracked the Li is only present near the mouth of the crack at the plating electrode interface. Modified from ref.[29] with the image on the left indicating the two planes over which the zoom-ins are shown. b) Scanning electron microscope (SEM) image and X-ray CT reconstruction of a crack within LLZO showing that the crack is partially filled with Li. Data reconstructed from measurements taken in ref. [30].

the elastic opening of the crack and the electrochemical forces that govern the filling of cracks.

2. Problem Definition and a Variational Principle for Crack Growth

The penetration of Li into Li-stuffed ceramic single-ion conductor electrolytes occurs from the Li metal electrode that is being plated. There exists significant controversy in the literature on the geometry of the dendrite/Li filament (is it a crack or a dislocation-like defect?) and whether the fractured electrolyte is fully filled with Li or not. Here, we shall develop a variational principle where the geometry of the dendrite/crack and the extent of filling are outcomes of the coupled electromechanical kinetics. The key outcomes of the analysis will include: 1) the conditions under which dendrites/cracks grow and 2) the mode of growth of the dendrites/cracks. For consistency of terminology throughout this study, we shall refer to the defect within the electrolyte as a crack and the Li within this crack as the Li filament. We do this to avoid confusion with the term dendrite which typically has been used to describe a defect that is fully filled with Li.

In line with many experiments that investigate crack growth in solid electrolytes, we consider a symmetric cell as shown in **Figure 2a** with an external power source imposing a voltage difference Φ_p between the two electrodes. A pre-existing crack of length a_0 in the single-ion conductor electrolyte is assumed to emanate from the interface of the plating Li electrode

(inset of Figure 2a) and we develop a kinetic framework for investigating the response of this cell in terms of the growth of this pre-existing crack. Such cracks which are typically on the order of the grain size are well-known to exist in all engineering ceramics and hence it is reasonable to assume that the problem is related to the conditions for the growth of cracks rather than the nucleation of defects. We shall make three simplifying assumptions that are commonly employed for problems of this type: 1) The electrolyte remains electroneutral such that every Li^+ cation is paired with an immobile anion within the single-ion conductor electrolyte. Thus, the Li^+ occupancy in the electrolyte is spatially uniform and flux is driven purely by the electric potential gradient. A charged Debye layer on the order of 1 nm or less might form at the electrode/electrolyte interface but this is accounted in the measured electrode/electrolyte interface resistance; 2) The molar volume Ω_e of Li within the electrolyte is assumed to be zero^[21,26] because the Li in Li-stuffed ceramic electrolytes lies within a rigid ceramic skeleton that does not deform upon removal/addition of a Li atom; and 3) The electrolyte remains thermodynamically stable at the operating temperatures and pressures with any stability of the electrolyte with respect to the Li metal electrode accounted for by interface resistance between the electrode and electrolyte.

In addition, it will be shown that the Li filaments within the cracks are less than 100 nm in thickness. Recent micropillar compression tests^[31–33] suggest that Li pillars in the micrometer length scale have a uniaxial yield strength σ_Y above 100 MPa. Direct measurements^[34] of stresses in the electrolytes around

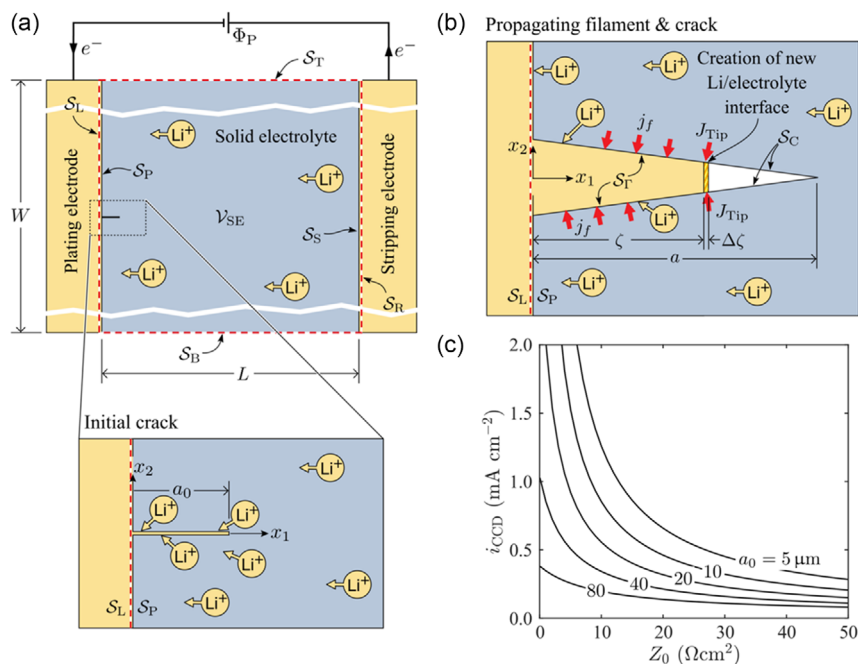


Figure 2. a) Sketch of the symmetric cell analyzed with the system of volume \mathcal{V} that is bounded by $\mathcal{S} \equiv S_L \cup S_R \cup S_T \cup S_B$. The electrolyte of size $L \times W$ has a volume labeled \mathcal{V}_{SE} and the plating and stripping electrode interfaces are labeled S_P and S_S , respectively. There exists an initial crack of length a_0 that is perpendicular to S_P . b) Sketch showing the plating of the Li at the tip of the filament with a current J_{Ttip} along with the current density $j_f = j_f n_f$ across the crack flanks along with crack surface S_T along which the Li filament of length ζ is present with the remainder of the crack of length a being dry. The dry crack flanks are labeled S_C . c) Predictions of the CCD i_{CCD} as a function of electrode/electrolyte interface resistance Z_0 for selected values of a_0 using properties representative of LLZO (Table 1).

cracks also suggest stresses on the order of 150 MPa. Taken together, this strongly suggests that Li within the crack is much stronger than bulk Li that creeps at a stress on the order of 1 MPa at room temperature.^[32] Given the high stresses that Li filaments can sustain within cracks, we shall idealize the Li within the filaments as rigid.

Our aim is to analyze the growth of cracks and Li filaments within the electrolyte and to do so we define a system that occupies a domain \mathcal{V} , as shown in Figure 2a. This system excludes the external power supply but encompasses the entire electrolyte volume \mathcal{V}_{SE} and an infinitesimal layer of each electrode. Both metal electrodes are maintained at fixed electrical potentials by the external power supply and this sets known boundary conditions for the system being analyzed. While this is the simplest system that can be analyzed for investigating the growth of cracks, it is nevertheless a complex open system with fluxes of Li^+ ions across left and right boundaries of the system that are adjacent to the stripping and plating electrolyte/electrode interfaces \mathcal{S}_S and \mathcal{S}_P , respectively, a change in the total Li content in the system as the Li filaments grow due to Li^+ ions being deposited into the crack, a net flux of electrons from the plating electrode to neutralize the Li^+ ions being deposited into the crack, and storage of elastic energy within the electrolyte associated with opening of the crack.

2.1. Brief Description of the Variational Principle

Here we briefly describe the salient features of the variational principle with full details and mathematical derivations provided in Section S1, Supporting Information. The kinetic variational principle makes use of the Onsager^[35,36] formalism wherein the rate of loss of potential energy $\dot{\Pi}$ of the system drives the dissipation within the system. We treat the electroneutral single-ion conductor electrolyte as an isotropic linear dielectric with permittivity ϵ_{SE} and a conductivity κ for Li^+ ions. The electrolyte is also an isotropic linear elastic solid with shear modulus G and Poisson's ratio ν such that the stiffness tensor is $\mathbb{C}_{ijkl} = 2G\nu\delta_{ij}\delta_{kl}/(1-2\nu) + G(\delta_{ik}\delta_{jl} + \delta_{il}\delta_{jk})$, where δ_{ij} is the Kronecker delta and the stress σ_{ij} is related to the strain $\epsilon_{ij} \equiv (u_{i,j} + u_{j,i})/2$ via $\sigma_{ij} = \mathbb{C}_{ijkl}\epsilon_{kl}$ where u_i is the displacement field within the electrolyte. While the formulation is general and can be employed for a 3D system with an arbitrary crack shape, here for simplicity we shall describe the formulation in a 2D plane strain setting in the $x_1 - x_2$ plane with a crack growing in the x_1 -direction constrained to remain straight. Consider the system at a general time t such that a crack of length a and Li filament of length ζ exists within the electrolyte of thickness L and width W , as shown in Figure 2a. Initially, at $t = 0$, the filament is of infinitesimal thickness and equal to the initial crack length a_0 , that is, $\zeta = a_0$. The voltage difference Φ_p is imposed at $t=0$. The origin of the co-ordinate system is located at the mouth of the crack on the electrolyte/plating electrode interface and the x_1 -direction is perpendicular to the interface, as shown in Figure 2a. We shall assume that an electron-conducting pathway always exists over the entire length of the filament.

Contributions to the rate of change $\dot{\Pi}$ of a potential energy arise from: 1) the rate of change \dot{N}_{Li} of Li content within the

system; 2) the rate of change of electrical energy associated with the electric field E_i and electric displacement D_i where $D_i = \epsilon_{SE}E_i$; 3) the current density j_i of Li^+ ions across the left and right system boundaries \mathcal{S}_L and \mathcal{S}_R shown in Figure 2a and the current density j_i^{el} of electrons from the plating electrode; 4) the rate of change \dot{U}_{elas} of elastic energy of the electrolyte; and 5) the changes in the surface energy due to fracture of the electrolyte in terms of the fracture energy γ_{SE} and the adhesion energy γ_{adh} associated with the formation of new Li/electrolyte interfaces on the crack flanks. $\dot{\Pi}$ follows as (Section S1.3, Supporting Information)

$$\begin{aligned} \dot{\Pi} = & \dot{N}_{\text{Li}}\mu_0 - \int_{\mathcal{V}} D_i \dot{E}_i d\mathcal{V} - \int_{\mathcal{S}_T \cup \mathcal{S}_B} D_i n_i \dot{\phi} dS + \dot{U}_{\text{elas}} \\ & - \int_{\mathcal{S}} T_i \dot{u}_i dS + \frac{1}{F} \int_{\mathcal{S}_L} \mu_{\text{Li}^+} j_i n_i dS + \frac{1}{F} \int_{\mathcal{S}_R} \mu_{\text{Li}^+} j_i n_i dS \\ & - \frac{1}{F} \int_{\mathcal{S}_L} \mu_{\text{el}} j_i^{\text{el}} n_i dS - 2\gamma_{\text{adh}} \dot{\zeta} + 2\gamma_{SE} \dot{a} \end{aligned} \quad (1)$$

where μ_{el} and μ_{Li^+} are the chemical potentials of the electrons and Li^+ ions, respectively, that leave/enter the system at electrode/electrolyte interfaces with outward unit normal n_i , μ_0 is the chemical potential of Li metal, and F is the Faraday constant. Note that boundary integrals over the top and bottom free surfaces of the electrolyte \mathcal{S}_T and \mathcal{S}_B are included as D_i is specified on these surfaces while tractions specified over the entire surface $\mathcal{S} \equiv \mathcal{S}_L \cup \mathcal{S}_B \cup \mathcal{S}_R \cup \mathcal{S}_T$ of the system. Mass conservation dictates that

$$\int_{\mathcal{S}_L} j_i n_i dS + \int_{\mathcal{S}_R} j_i n_i dS = -\dot{N}_{\text{Li}} F \quad (2)$$

while the requirement that the system remains charge neutral relates \dot{N}_{Li} to the electron flux via

$$\int_{\mathcal{S}_L} j_i^{\text{el}} n_i dS = \dot{N}_{\text{Li}} F \quad (3)$$

In order to set up the Onsager principle, we also need to consider the sources of dissipation in the system and thereby define a dissipation potential \mathcal{D} . The four sources of dissipation within the system are: 1) Li^+ flux through the solid electrolyte of conductivity κ , 2) the resistance Z_0 for the Li^+ flux across the electrode/electrolyte interfaces, 3) the resistance Z_f for the Li^+ flux across the crack flank, and 4) the resistance R_{Tip} for Li^+ to acquire an electron at the tip of the Li filament as it forms a new Li/electrolyte interface on the crack flanks; see Figure 2b. Consequently, the dissipation potential is defined by (Section S1.3, Supporting Information)

$$\begin{aligned} \mathcal{D} = & \frac{1}{2} \left[\frac{1}{\kappa} \int_{\mathcal{V}_{SE}} j_i j_i d\mathcal{V} + Z_0 \int_{\mathcal{S}_P} j^2 dS + Z_0 \int_{\mathcal{S}_S} j^2 dS \right. \\ & \left. + Z_f \int_{\mathcal{S}_\Gamma} j^2 dS + 2R_{\text{Tip}} J_{\text{Tip}}^2 \right] \end{aligned} \quad (4)$$

where $j = j_i n_i$ and \mathcal{S}_Γ is the portion of the crack flanks over which the Li filament is present (inset of Figure 2a) with n_i the outward

unit normal to the electrolyte. In addition, J_{Tip} is the Li^+ current to the tip of the Li filament through each of the two crack flanks (symmetry dictates that the currents across the two flanks are equal), while conservation of Li dictates that the filament extends by a rate $\dot{\zeta} = 2J_{\text{Tip}}/(F\rho_m\delta_{\text{Tip}})$ where ρ_m is the molar density of Li and δ_{Tip} is the crack opening at the tip of the filament (inset of Figure 2a). Note that Z_0 and Z_f are assumed to be constants, implying a linearized form of Butler–Volmer kinetics across the electrode/electrolyte interfaces and the crack flanks.

The rate of change of potential energy (1) is combined with the dissipation potential (4) to define an augmented potential $\dot{\Psi} = \dot{\Pi} + \mathcal{D}$ in terms of the independent field variables $(\hat{u}_i, \dot{a}, j_i, J_{\text{Tip}}, \dot{\varphi})$ where φ is the electric potential and, \hat{u}_i is the time derivative of the displacement field at constant crack length, as defined in Section S1.3, Supporting Information. The Onsager principle^[35] demands that the system evolves such that the fields satisfy $\delta\dot{\Psi} = 0$ at every instant. This requirement delivers the strongly coupled electromechanical governing partial differential equations and associated boundary conditions for the problem, as derived in Section S1.3, Supporting Information.

The governing equation for the electric field within the electrolyte \mathcal{V}_{SE} is the electroneutral Gauss law given by $\hat{\varphi}_{,ii} = 0$ where $\hat{\varphi} = \varphi + \mathcal{U}$ and \mathcal{U} is the open-circuit potential between the electrolyte and Li metal. The boundary conditions associated with this Laplace equation are $D_i n_i = j_i n_i = 0$ on the lateral boundaries \mathcal{S}_T and \mathcal{S}_B (Figure 2a), where $j_i = -\kappa\hat{\varphi}_{,i}$ while the flux of Li^+ through the electrode/electrolyte interfaces satisfies

$$j_i n_i = \frac{\hat{\varphi} - \Phi_P}{Z_0} \text{ on } \mathcal{S}_S \quad \text{and} \quad j_i n_i = \frac{\hat{\varphi}}{Z_0} \text{ on } \mathcal{S}_P \quad (5)$$

In contrast, on the crack flank \mathcal{S}_f where the Li filament is present, the flux boundary conditions involve the tensile stress σ_n across the interface via

$$j_f \equiv j_i n_i = \frac{1}{Z_f} \left(\hat{\varphi} + \frac{\sigma_n}{F\rho_m} \right) \quad (6)$$

where n_i is the unit normal to the crack flank pointing into the crack. This boundary condition couples the solution of the electric field within the electrolyte to the mechanical problem. In addition, the electric field/potential within the electrolyte needs to admit a current sink of magnitude

$$J_{\text{Tip}} = \frac{1}{R_{\text{Tip}}} \left[\hat{\varphi}_{\text{Tip}} + \left(\frac{2\gamma_{\text{adh}}}{F\rho_m\delta_{\text{Tip}}} \right) \right] \quad (7)$$

at the Li filament tip of thickness δ_{Tip} located at ζ (Figure 2b): this current sink lengthens the Li filament. Here, $\hat{\varphi}_{\text{Tip}}$ is the value of $\hat{\varphi}$ in the vicinity of the filament tip within the electrolyte. This boundary condition requires special consideration as the existence of the sink implies a singularity in $\hat{\varphi}$, and a superposition methodology is used to solve for this singularity, as detailed in Section S2, Supporting Information.

Similarly, $\delta\dot{\Psi} = 0$ delivers the mechanical balance laws within the electrolyte, that is, the static equilibrium equation $\sigma_{ij,j} = 0$ along with the associated boundary conditions. These boundary

conditions are as follows: 1) the crack opening displacement δ_{Li} at time t along \mathcal{S}_f is given by mass conservation as

$$\delta_{\text{Li}}(x_1, t) = \frac{2}{F\rho_m} \int_{\tau(x_1)}^t j_f(x_1, t') dt' \quad (8)$$

where j_f follows from (6) and $\tau(x_1)$ is the time at which the filament tip ζ is first located at x_1 and 2) on all other electrolyte boundaries, that is, $\mathcal{S}_S, \mathcal{S}_P, \mathcal{S}_T, \mathcal{S}_B$ and the crack flank \mathcal{S}_C where the Li filament is absent, the tractions vanish such that $T_i = 0$. Additionally, $T_1 = 0$ over \mathcal{S}_f (i.e., zero shear tractions between the Li filament and the electrolyte). The solution of $\sigma_{ij,j} = 0$ with these boundary conditions delivers the mechanical fields within the electrolyte for a given crack length a . It is emphasized that this mechanical solution requires a solution coupled with Gauss's law. In addition, the Onsager principle delivers the time evolution of crack length via the Griffith^[37] condition

$$\gamma_{\text{SE}} = - \left. \frac{\partial U_{\text{elas}}}{\partial a} \right|_{u_2 \in \mathcal{S}_f} \quad (9)$$

where

$$U_{\text{elas}} = \frac{1}{2} \int_{\mathcal{V}_{\text{SE}}} \varepsilon_{ij} C_{ijkl} \varepsilon_{kl} d\mathcal{V} \quad (10)$$

is the elastic strain energy within the electrolyte. Details of the derivations are given in Section S1.3, Supporting Information with material parameters for the LLZO electrolyte shown in **Table 1**. This highly coupled electromechanical formulation not only predicts the CCD i_{CCD} but also the kinetics of crack and Li filament growth, including the shapes of the crack and Li filament, for operation of the cell at a current density $> i_{\text{CCD}}$. Details of the numerical scheme to solve these coupled equations are provided in Section S2, Supporting Information. We emphasize here that while the above formulation has been presented for a symmetric cell, the predictions are not restricted to a symmetric cell especially when presented in terms of the cell current. This is similar to the case of the symmetric cells used in experiments where measurements of Li filament growth when presented in terms of cell current apply equally to a nonsymmetric cell.

2.2. The Critical Current Density

The above equations considerably simplify for the case of a non-propagating crack and can then be used to deduce the CCD i_{CCD} . At an imposed cell current density magnitude $i_{\infty} \leq i_{\text{CCD}}$, the pre-existing crack fills with Li and a steady-state is attained where Li^+

Table 1. Summary of material parameters for the LLZO electrolyte.

Material parameter	Symbol	Value	References
Conductivity of LLZO	κ	0.46 mS cm ⁻¹	[9]
Shear modulus of LLZO	G	60 GPa	[43]
Poisson's ratio of LLZO	ν	0.2	[43]
Surface adhesion energy between LLZO/Li	γ_{adh}	0.22 J m ⁻²	[11]
Surface energy of LLZO	γ_{SE}	0.84 J m ⁻²	[11]

flux across the crack flanks is switched-off, that is, from (6) $\sigma_n = -F\rho_m\hat{\phi}$. As the pre-existing crack is assumed to contain lithium along its entire length, there can be no lithium flux into its tip until the crack is forced to propagate. Moreover, with no Li flux into the crack, the solution of Gauss's law within the electrolyte is trivial as the Li^+ flux within the electrolyte is 1D in the x_1 -direction. Thus, $\hat{\phi}$ is given by

$$\hat{\phi} = i_\infty \left[Z_0 + \frac{x_1}{\kappa} \right], \quad (11)$$

where $i_\infty = \Phi_p / (2Z_0 + (L/\kappa))$ is the magnitude of the cell current density (i.e., the current per unit electrode/electrolyte interface area) and L is the thickness of the electrolyte. The calculation of i_{CCD} then is simplified considerably for the case of an initial crack of length a_0 that emanates perpendicular from the plating electrode/electrolyte interface. From (6) and (11) it follows that the crack opening traction varies as

$$T_n = -\sigma_n = T_0 + \frac{T_0 x_1}{\kappa Z_0}, \quad (12)$$

where $T_0 = F\rho_m i_\infty Z_0$. Given this traction distribution along the crack flanks, for the practical case of $a_0/L \rightarrow 0$, there exists a closed-form solution for (9) given in Tada et al.^[38] At $i_\infty = i_{\text{CCD}}$, the relation in (9) is satisfied, and therefore the crack and filament propagate, when

$$T_0 \sqrt{\pi a_0} \left[1.122 + \frac{0.683 a_0}{\kappa Z_0} \right] = \sqrt{\frac{4G\gamma_{\text{SE/Li}}}{(1-\nu)}} \quad (13)$$

where $\gamma_{\text{SE/Li}} = \gamma_{\text{SE}} - \gamma_{\text{adh}}$ is the surface energy of an electrolyte/Li interface. Re-arranging (13), a closed-form expression for i_{CCD} follows as

$$i_{\text{CCD}} = \frac{1}{F\rho_m} \sqrt{\frac{4G\gamma_{\text{SE/Li}}}{(1-\nu)\pi a_0}} \left[1.122 Z_0 + \frac{0.683 a_0}{\kappa} \right]^{-1} \quad (14)$$

Note that in (13-14) we have employed $\gamma_{\text{SE/Li}}$ rather than γ_{SE} as at incipient crack propagation at i_{CCD} we anticipate the crack and Li filament to propagate in unison since $\gamma_{\text{SE/Li}} < \gamma_{\text{SE}}$ ($\gamma_{\text{adh}} > 0$; see Table 1). The predicted variation (14) of i_{CCD} with electrode/electrolyte interface resistance Z_0 is included in Figure 2c for selected choices of the initial crack length a_0 and using material parameters representative of the LLZO electrolyte, as listed in Table 1. In line with numerous observations, the model predicts a reduction in i_{CCD} with increasing Z_0 and of course with increasing initial crack length a_0 . The reduction in i_{CCD} with increasing Z_0 follows from the fact that a higher Z_0 induces higher crack-opening tractions T_n due to a higher electric potential within the electrolyte relative to the plating electrode; see Equation (12).

Equation (14) succinctly captures some variables that affect i_{CCD} and can be used to guide design. For example, we observe that i_{CCD} increases with decreasing κ and Z_0 which are both variables that can be adjusted by via the electrochemistry of the electrolyte. Similarly, i_{CCD} increases with the modulus G and the surface energy $\gamma_{\text{SE/Li}}$ but these material parameters are typically difficult to influence by processing routes. On the other hand, there is a strong influence of initial flaw size a_0 on i_{CCD}

(Figure 2c). It is well established that a_0 in engineering ceramics scales with the grain size but improved sintering routes in processing are expected to reduce a_0 and our model will then predict higher values of i_{CCD} . We emphasize here that our analysis assumes a perfect Li plating electrode in which no voids have grown at the electrode/electrolyte interface. During stripping, voids are known to form at the interface with dendrites then preferentially growing during plating from the vicinity of these voids.^[13-16] These voids are suppressed by stack pressure. Since our current analysis assumes a defect-free Li metal electrode, there is no dependency of stack pressure in this analysis.

3. Growth of Cracks in LLZO

Cracks grow in LLZO such that they are sparsely filled with Li^[30] but given the very small shorting times of the cells,^[10] it is reasonable to assume that the cell shorts soon after the crack fully penetrates the entire thickness of the electrolyte. Thus, the Li filament and crack extend in unison in LLZO with $\zeta \approx \hat{a}$. In our formulation, this is achieved by setting $R_{\text{Tip}} = 0$ and we shall investigate the effect of $R_{\text{Tip}} > 0$ in Section 4. The justification for the choice $R_{\text{Tip}} = 0$ in LLZO is based on the fact that density functional theory (DFT) calculations^[39] show that LLZO surfaces have a much smaller bandgap compared to the bulk and thus trap a significant number of excess electrons. This implies that as Li^+ is deposited near the tip of the filament (Figure 2b), it easily acquires electrons, resulting in negligible resistance to the plating of Li metal at the filament tip. All calculations in this and subsequent sections are reported for an electrolyte of size $L \times W = 1 \text{ mm} \times 3 \text{ mm}$, which is representative of the electrolyte used in many reported experiments.^[28-30] In engineering ceramics, flaws/cracks on the order of grain size commonly exist. Given that the grain sizes of LLZO sintered at temperatures in the range 1100 – 1200 °C are typically in the range 15 – 30 μm ,^[40] in the calculations, we assume an initial flaw of length $a_0 = 25 \mu\text{m}$ that emanates normally from the plating Li electrode/electrolyte interface and initially only contains an infinitesimally thin layer of Li. The electrode/electrolyte resistance is taken to be $Z_0 = 5 \Omega\text{cm}^{2[9]}$ and in the absence of direct measurements we assume that the crack flank/Li filament resistance $Z_f = Z_0$. The calculations have been conducted by imposing a potential difference Φ_p across the electrodes and we report the results in terms of the imposed cell current density magnitude $i_\infty = \Phi_p / (L/\kappa + 2Z_0)$, which is the current in the absence of the growth of the Li filament: the large width W of the electrolyte employed in the calculations implies that the growth of the Li filament has a negligible effect upon the average cell current i_∞ .

3.1. The Effect of Mismatch Between Elastic Crack Opening and Li Flux into the Crack

For cracks of initial length $a_0 = 25 \mu\text{m}$, the CCD $i_{\text{CCD}} = 0.71 \text{ mAcm}^{-2}$ according to Equation (14). Now consider the case of an imposed current density of $i_\infty = 1 \text{ mAcm}^{-2} > i_{\text{CCD}}$ such that the crack and accompanying Li filament both extend. Predictions of the length of the crack

and Li filament at three selected times t are shown in **Figure 3**. In **Figure 3a**, we include distributions of normalized current density $\hat{j} \equiv \sqrt{j_f i_\infty}$ while the corresponding distributions of the σ_{22} stress component are shown in **Figure 3b** (also see Video S1, Supporting Information). First consider **Figure 3a** which includes a quiver plot to show the direction of the Li^+ flux within the electrolyte and the shape of the crack (the opening of the crack has been magnified by two orders of magnitude so that the shape/profile is visible). Note that the Li filament fills the crack, as depicted by shading the crack black. The crack profiles in **Figure 3a,b** indicate that the crack opening is maximum near the midlength of the crack. (In contrast, the maximum opening along the length of an internally pressurized crack is typically at the crack mouth.) Throughout its loading history, the crack-opening rate is positive over the entire length of the crack, that is, the crack continues to thicken monotonically (i.e., open) consistent with observations in ref. [29]. Thus, the bulged shape of the

crack-opening profile necessarily arises from the spatial variation of the Li^+ flux into the crack.

The spatiotemporal distributions of \hat{j} included in **Figure 3a** show that far ahead of the crack tip the current density is spatially uniform and 1D within the electrolyte with $\hat{j} = 1$. Nearer the crack, the Li^+ flux across the crack flanks implies that the flux field is no longer 1D with the current density achieving a maximum around the crack tip. While the flux magnitude decreases toward the plating electrode/electrolyte interface it is difficult to infer directly the current density j_f into the crack from these distributions of \hat{j} . Predictions of the normalized crack flank current density j_f/i_∞ are shown in **Figure 3c** at three selected times and clearly show that the crack flank flux is a maximum at the tip and monotonically decreases toward the crack mouth at the plating electrode interface. Qualitatively we would expect such a dependence as the overpotential $\hat{\phi}$ in (6) is expected to decrease with decreasing x_1 ; see for example the dependence (11) of $\hat{\phi}$ on x_1 in

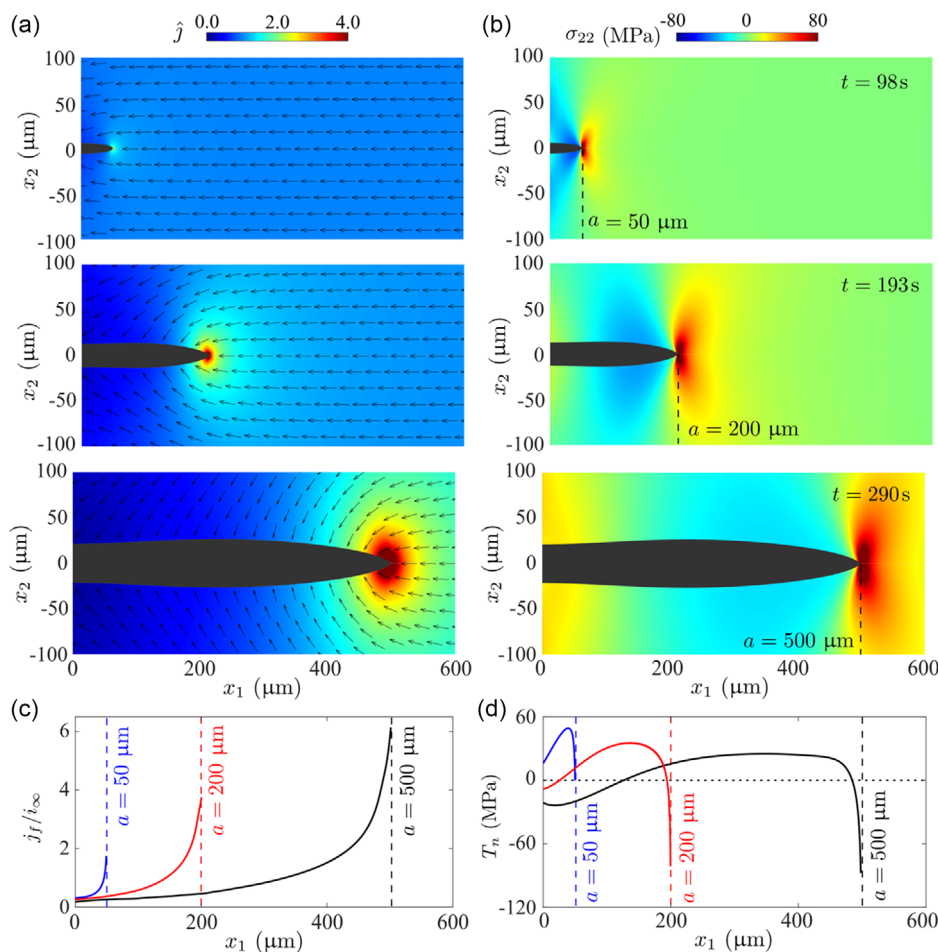


Figure 3. Predictions of the evolution of the a) normalized current density $\hat{j} \equiv \sqrt{j_f i_\infty}$ and b) stress σ_{22} within the electrolyte for a cell with $R_{Tp} = 0$ subjected to an imposed current density $i_\infty = 1 \text{ mAcm}^{-2}$. In (a) we include a quiver plot to show the direction of Li^+ flux within the electrolyte. Debonding of the Li from the crack flanks is not permitted. The opening of the crack is magnified $\times 200$ so that the crack profile is clearly visible. The time t and current crack length a are indicated for each of the three time instants (also see Video S1, Supporting Information). Corresponding predictions of the c) normalized crack flank current density j_f/i_∞ and d) crack flank tractions T_n . Note that a positive value of T_n contributes to opening the crack whereas a negative one does the opposite.

the absence of flux into the growing Li filament. Now recall from (8) that the crack opening depends upon both the current density j_f and the time interval over which the crack faces exist. The bulged opening arises from the fact that while j_f decreases toward the plating electrode interface (and thereby tends to decrease δ_{Li}), τ also decreases with $\tau = 0$ for $x_1 \leq a_0$ and this tends to increase δ_{Li} .

The σ_{22} stress distributions included in Figure 3b clearly show the high stresses associated with the crack tip stress intensity factor. More intriguing is the change in sign of σ_{22} along the crack flank. Recall that σ_{22} is related to the tractions on the crack flank by $T_n = -\sigma_{ij}n_jn_i$ where n_i is the unit normal to the crack flank pointing into the crack. Note that the definition of T_n means that its positive sense is in the direction of the inward normal to the electrolyte. It follows that $T_n = -\sigma_{22}|_{x_2=0, x_1 \leq a}$ where a is the current length of the crack and a negative T_n implies that the crack flank tractions are attempting to close rather than open the crack. These crack flank tractions are plotted in Figure 3d for the three times t shown in Figure 3b. Early in the loading history when the crack has propagated to $a = 50 \mu\text{m}$, the tractions remain positive indicating that the Li that fluxes into the crack is tending to open the crack over its entire length. With increasing time (and crack length a), while the qualitative form of the T_n distribution remains similar, important quantitative differences emerge. The traction T_n becomes negative near the crack mouth and tip, indicating that the Li within the crack is attempting to close the crack at these locations. In this analysis, we have assumed that the crack opening is set by (8) and thus equal to the time-integrated total Li^+ flux at any location along the crack. The calculations show that with the crack-opening set by the time-integrated Li^+ flux, elasticity of the electrolyte then requires the Li within the crack to close rather than open the crack at some locations and here the crack flank tractions become negative. This is most clearly seen in terms of the crack profile where the crack opening is lower near the crack mouth compared to

that at midlength of the crack—this lower crack mouth opening is a direct consequence of the negative T_n near the crack mouth.

Note that the spatial gradients in Li^+ flux along the length of a crack exist for dendrites in liquid electrolytes. However, negative dendrite flank tractions do not develop in liquid electrolytes as liquids deforms with a vanishing deviatoric stress. Thus, dendrites in liquid electrolytes can take mushroom-like shapes with them bulging away from the plating electrode interface^[41] but yet maintain compressive Li stresses (positive pressure) within the dendrite.

3.2. Debonding of Crack Flank/Li Filament

The finite shear modulus of a solid electrolyte implies that the negative crack flank tractions shown above are commonplace if we assume that the crack opening is set by the Li^+ flux into the crack at every location along its flank. These negative tractions are on the order of at-least 25 MPa (Figure 3d) and the interface between the electrolyte and the Li filament needs to sustain a tensile traction of this order if this crack/Li filament propagation mode is to exist. The adhesive strength between Li and LLZO is on the order of a few kPa^[42] and thus a better approximation is that the Li/electrolyte interface along the crack flank can only sustain compressive tractions. We therefore modify the formulation summarized in Section 2 to include the constraint that $T_n(x_1) \geq 0$. Specifically, we modify the boundary conditions for the stress equilibrium equation $\sigma_{ij,j} = 0$ over S_Γ to be a contact-type boundary condition, that is, over S_Γ the crack opening $\delta(x_1) = \delta_{\text{Li}}(x_1)$ where δ_{Li} is given by (8) if $T_n(x_1) \geq 0$; otherwise, $T_n(x_1) = 0$ and the crack opening $\delta(x_1) > \delta_{\text{Li}}(x_1)$ is an outcome of the solution of the elasticity problem; see Section S3, Supporting Information for further details.

The temporal evolution of the debonding of the Li filament from the electrolyte is a complex phenomenon that ultimately results in a complicated structure of a partially filled crack as

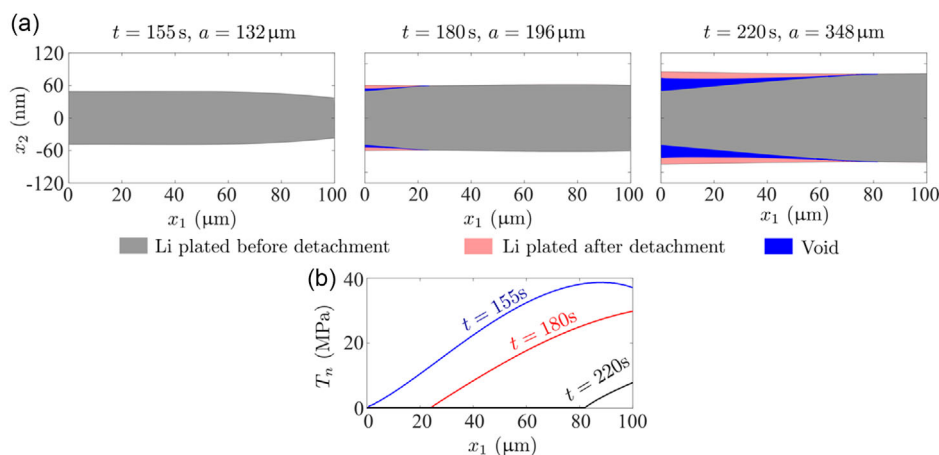


Figure 4. Structure of the Li filament within the crack near the crack mouth for the case of a cell subjected to an imposed current density $i_\infty = 1 \text{ mAcm}^{-2}$ with $R_{\text{tip}} = 0$. a) The Li within the crack at three time instants with $t = 155 \text{ s}$ corresponding to the instant when debonding is about to commence at the crack mouth. Subsequently we show the Li filament geometry within the crack with the shading indicating the empty regions and Li deposited before and after detachment from the crack flanks. Note that the x_2 -axis scale is in nanometers such that the crack opens by less than 100 nm when it has propagated to a length $a \approx 350 \mu\text{m}$. b) The corresponding evolution of the crack flank tractions T_n that are not permitted to be negative.

observed via X-ray CT for LLZO.^[30] To illustrate this, we consider the case analyzed in Section 3.1 and first illustrate the process by which the Li filament detaches from the electrolyte that results in partial filling of the crack near the crack mouth. The shape of the crack near its mouth is shown in **Figure 4a** at three selected times, with the crack lengths also indicated. At $t = 155$ s, the crack is fully filled with Li over the region shown but the corresponding spatial distribution of T_n shown in **Figure 4b** suggests that the crack flanks are about to debond from the Li filament at the mouth ($x_1 = 0$) as $T_n(x_1 = 0) = 0$. When debonding occurs we assume that an atomistically thin layer of Li is left adhered to the electrolyte flanks so that further Li^+ flux into the crack can continue with the fluxing Li^+ acquiring an electron from this layer that is connected to the plating electrode. This continued flux gives a Li deposition rate $\dot{\delta}_{\text{Li}} < \dot{\delta}$ with the traction being maintained at $T_n = 0$ at $x_1 = 0$. In fact, with increasing time, the debonding progresses toward the crack tip (i.e., $x_1 > 0$) and the expected Li filament structure within the crack and the corresponding traction distribution are plotted in **Figure 4** at $t = 180$ s. At this instant, $T_n = 0$ for $x_1 < 20 \mu\text{m}$ and this portion of the crack is partially filled with Li. In **Figure 4a**, we shaded the crack volume to show three separate regions: 1) Li deposited before detachment is shaded grey; 2) Li deposited after detachment is shaded pink; and 3) a void or empty region is shaded blue. We emphasize that we have assumed that the Li within the crack is rigid. This implies that we are unable to predict the precise Li filament morphology within the partially filled crack. The Li morphology shown in **Figure 4a** assumes that the Li does not deform and thus the voided region is shown in **Figure 4a** between the Li that was initially deposited (grey in **Figure 4a**) and the Li that is deposited after detachment occurred (shaded pink in **Figure 4a**). Nevertheless, it is clear from **Figure 4a** that the extent of the empty region is largest at $x_1 = 0$ (see structure at time $t = 220$ s). This is a direct consequence of the fact that detachment first occurred at $x_1 = 0$ and that the crack-opening rates are the largest at the crack mouth.

The geometry of the Li filament within the partially filled crack shown in **Figure 4a** is inaccurate due to the assumption that the Li is rigid. However, our aim here is not to describe the Li filament geometry in detail but rather quantify the level of filling of the crack and its effect on crack propagation. Keeping this in mind, we define a filling ratio c of the crack with its rate of change given by

$$\dot{c}(x_1) = -\frac{1}{\delta(x_1)} \{ \dot{\delta}(x_1) - \dot{\delta}_{\text{Li}}(x_1) \}, \quad (15)$$

where $\{ \cdot \}$ denotes the Macaulay brackets and (15) is integrated at locations x_1 along S_Γ with initial conditions $c(x_1) = 1$. Then the crack flank tractions $T_n(x_1) \geq 0$ where $c(x_1) = 1$ and $T_n = 0$ where $c(x_1) < 1$. This coarse graining, whereby we only calculate the difference between the crack opening and deposition of Li, not only has the advantage of numerical convenience but also makes no assumptions about the geometry of the Li filament within the partially filled crack. Predictions using this approach are included in **Figure 5** (for the case analyzed for **Figure 3**) with flux distributions shown in **Figure 5a** and the corresponding stresses σ_{22} in **Figure 5b** (also see Video S2, Supporting Information). Two key differences are apparent: 1) in line with

typical crack-opening profiles, the opening increases monotonically behind the crack tip with the maximum opening at the mouth ($x_1 = 0$), and 2) the stresses σ_{22} do not change sign along the crack flanks. This is further clarified via the T_n distributions shown in **Figure 5c** where we see that the tractions vanish near the mouth and tip of the crack, that is, at locations where $T_n < 0$ in **Figure 3d**. At these locations where $T_n = 0$, the crack is partially filled with Li, as seen in **Figure 5d**, where we show the spatial distribution of the crack-filling ratio c for two selected crack lengths a .

The predictions that cracks in LLZO are partially filled with Li are consistent with recent X-Ray CT observations^[30] (see also **Figure 1b**) and our model gives a physical understanding of the phenomenon. When debonding of the Li filament from the electrolyte is permitted not only do partially filled cracks develop but negative tractions that tend to close the crack do not develop. These negative tractions tend to reduce the tip stresses (and stress intensity factor) and the absence of these negative tractions is expected to enhance crack growth rates. Predictions of the temporal evolution of the crack length a with time are included in **Figure 6a** for three imposed current densities i_∞ for the two sets of simulations, that is, 1) no debonding and 2) debonding permitted between the Li and the electrolyte along the crack flank. Clearly, when debonding is prevented, the growth of the crack slows down due to crack closing tractions (negative T_n) being imposed on the crack flanks near the tip and mouth of the crack. Predictions assuming no debonding and with debonding permitted of the average crack velocity $\langle \dot{a} \rangle$ (over the interval $150 \mu\text{m} \leq a \leq 250 \mu\text{m}$) as a function of i_∞ are included in **Figure 6b** along with corresponding measurements from Kazzyk et al.^[10] The predictions assuming full adhesion and no debonding underestimate the crack velocity while predictions that allow debonding with the crack flank tractions constrained to $T_n \geq 0$ agree remarkably well with the measurements. Thus, the predictions of partially filled cracks are not only consistent with direct tomographic observations of the Li filament structure within cracks but are also consistent with more macroscopic measurements of the growth rate of cracks. We emphasize here that the growth rate of the cracks is primarily governed by the current i_∞ with the electrolyte conductivity κ mainly influencing the cell voltage required to impose this current.

4. Growth of Dry Cracks

Ning et al.^[28] and Hao et al.^[29] used a combination of in-situ X-ray CT (see also **Figure 1a**) and spatially mapped X-ray diffraction to demonstrate that the crack tip in sulphide electrolytes outruns the Li filament such that cracks traverse the entire electrolyte with Li absent from the crack over a finite length behind the crack tip. Thus, cracking of the electrolyte can occur before the cell short circuits. In our model, we attribute the difference in behaviour of LLZO and sulfide electrolytes to a difference in the magnitude of the Li filament tip resistance R_{Tip} . DFT calculations^[39] have shown that the surface bandgap for sulfide electrolytes is large compared to the bulk and therefore we do not anticipate an accumulation of excess electrons on the surface of the fractured LPS. Consequently, we anticipate that a substantial

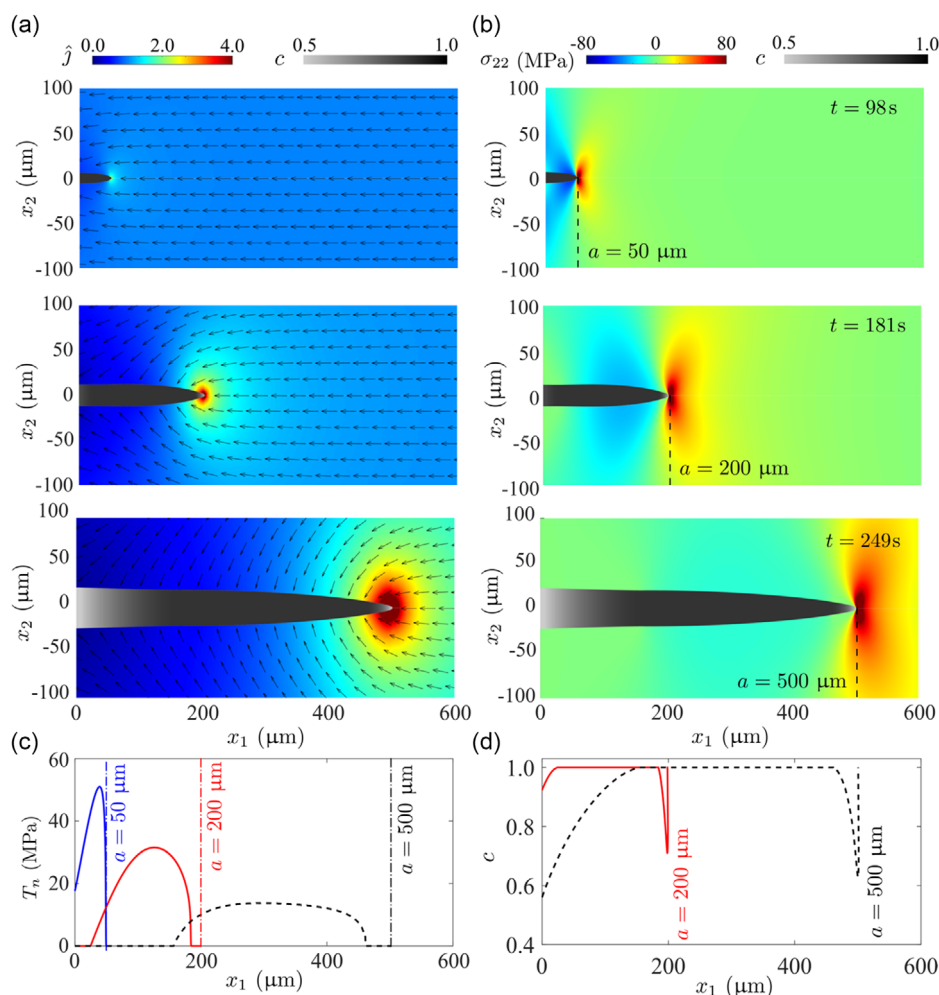


Figure 5. The effect of debonding between the Li filament and the crack flank on the predictions of the evolution of the a) normalized current density $\hat{j} \equiv \sqrt{j_j}/i_\infty$ and b) stress σ_{22} within the electrolyte for a cell with $R_{\text{Tip}} = 0$ subject to an imposed current density $i_\infty = 1 \text{ mA cm}^{-2}$. In (a) we include a quiver plot to show the direction of the Li^+ flux within the electrolyte. Debonding between the Li filament and crack flanks is assumed to occur such that the crack flank traction $T_n \geq 0$. The opening of the crack is magnified $\times 200$ so that the crack profile is clearly visible. The time t and current crack length a are indicated for each of the three time instants (also see Video S2, Supporting Information). Corresponding predictions of the c) crack flank traction T_n and d) filling fraction c along the crack.

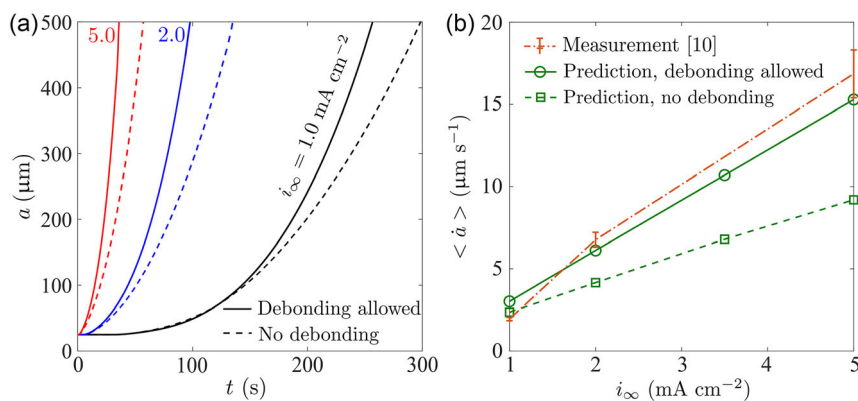


Figure 6. a) Predictions of the temporal evolution of the crack length a with $R_{\text{Tip}} = 0$ for three values of the imposed current density i_∞ . Results are shown for the cases when debonding is not permitted and when debonding of the Li from the crack flanks is allowed such that $T_n \geq 0$. b) Comparison between predictions and measurements^[10] of the average crack speed $\langle \dot{a} \rangle$ over the interval $150 \mu\text{m} \leq a \leq 250 \mu\text{m}$ as a function of i_∞ . The predictions for the both the debonding allowed and prevented cases are included.

resistance exists for Li^+ to acquire electrons near the Li filament tip (see Figure 2b) and expect that, unlike LLZO, $R_{\text{Tip}} \gg 0$ for sulphide electrolytes. While direct measurements of R_{Tip} have not been reported in the literature, we summarize the results of calculations here to show the effect of $R_{\text{Tip}} > 0$ on the growth of the crack and Li filament. The aim is to show the effect of R_{Tip} upon the mechanism of crack and Li filament propagation, and thus it suffices to keep all parameters fixed at the values for LLZO (Table 1) and only change R_{Tip} for the calculations reported in this section.

Predictions of the growth of the crack/Li filament initiating from an initial crack of length $a_0 = 25 \mu\text{m}$ are included in **Figure 7** (also see Video S3, Supporting Information). with the choice of $R_{\text{Tip}} = 22 \Omega\text{cm}$ (all loading parameters are the same as for the cases in Figure 3 and 5 and we restrict attention to the case when debonding is permitted such that $T_n \geq 0$). The high

value of R_{Tip} results in two major differences from the corresponding $R_{\text{Tip}} = 0$ results in Figure 5: 1) The Li filament and crack propagate simultaneously until $t \approx 90 \text{ s}$ ($a = \zeta \approx 50 \mu\text{m}$) but subsequently the crack tip accelerates ahead of the Li filament with the near-crack-tip region being devoid of Li. This is consistent with observations reported in ref. [29]; see Figure 3e. Thus, while the stress concentration persists near the crack tip, the flux concentration is no longer at the crack tip but further back and located at the Li filament tip. This is in contrast to the $R_{\text{Tip}} = 0$ case and 2) The crack propagation rate is lower compared to the $R_{\text{Tip}} = 0$ case. The crack propagates to $a = 500 \mu\text{m}$ in 250 and 315 s for $R_{\text{Tip}} = 0$ and $R_{\text{Tip}} = 22 \Omega\text{cm}$, respectively.

To understand the lower crack propagation rate, note that shorter Li filaments imply that the crack opening tractions are now exerted over a smaller fraction of the crack flank (compare Figure 7c with Figure 5c). Thus, the magnitudes of the tractions

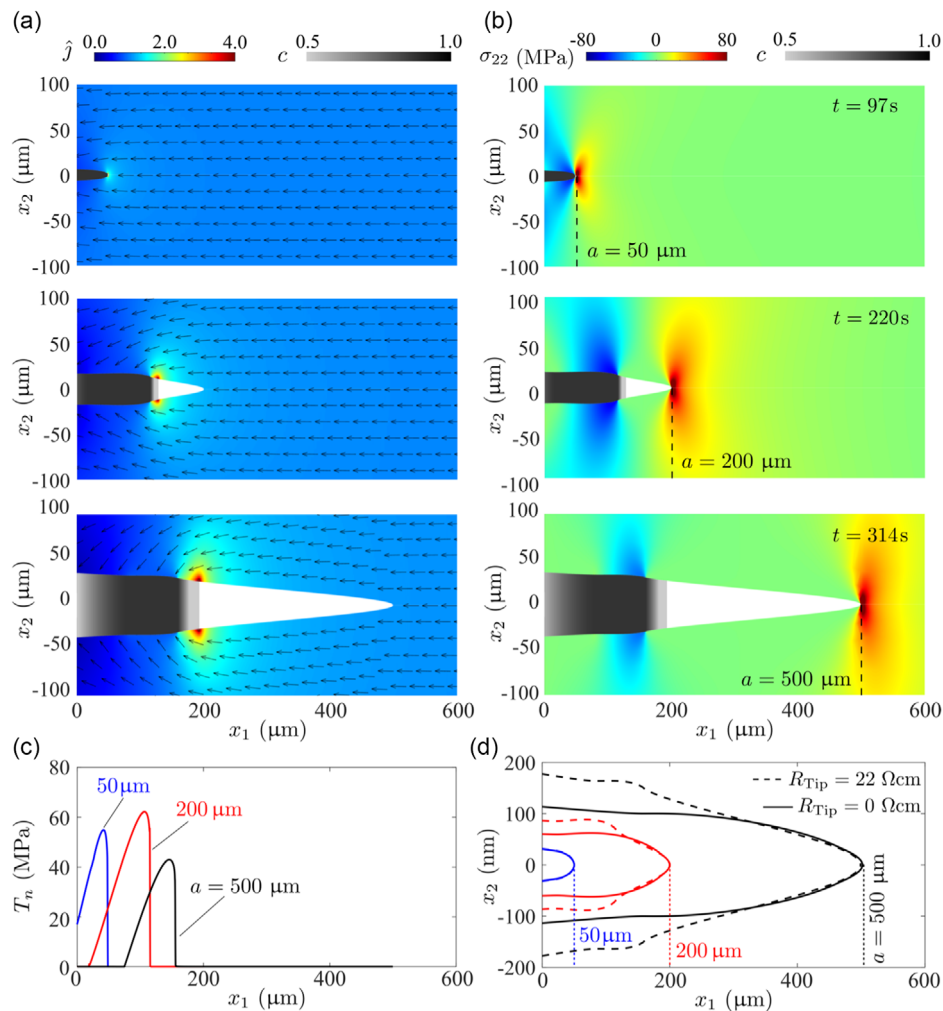


Figure 7. Predictions of the evolution of the a) normalized current density $\hat{j} \equiv \sqrt{j_i j_i} / i_\infty$ and b) stress σ_{22} within the electrolyte for a cell with $R_{\text{Tip}} = 22 \Omega\text{cm}$ subjected to an imposed current density $i_\infty = 1 \text{ mAcm}^{-2}$. In (a) we include a quiver plot to show the direction of the Li^+ flux within the electrolyte. Debonding is assumed to occur such that the crack flank traction $T_n \geq 0$. The opening of the crack is magnified $\times 200$ so that the crack profile is clearly visible. The time t and current crack length a are indicated for each of the three time instants (also see Video S3, Supporting Information). c) Corresponding predictions of the crack flank traction T_n and d) comparison of the crack profile for the $R_{\text{Tip}} = 22 \Omega\text{cm}$ case with the $R_{\text{Tip}} = 0$ case of Figure 5.

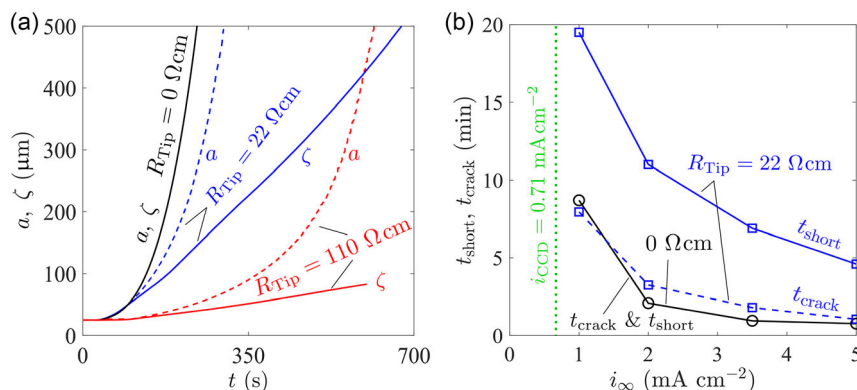


Figure 8. a) Predictions of the temporal evolution of the crack length a and Li filament length ζ for a cell subjected to an imposed current density $i_{\infty} = 1 \text{ mA cm}^{-2}$. Results are shown for three choices of the filament tip resistance R_{Tip} . b) Predictions of the time t_{crack} to crack the electrolyte and the time t_{short} to short the cell as a function of i_{∞} for two choices of R_{Tip} . These predictions are for an electrolyte of thickness $L = 1 \text{ mm}$.

need to be higher to allow the crack to propagate and these higher tractions requires greater crack openings, i.e. thicker Li filaments. To show this we compare the crack opening profiles for the $R_{\text{Tip}} = 0$ case from Figure 5 and the $R_{\text{Tip}} = 22 \Omega\text{cm}$ case in Figure 7d. Until $a \approx 50 \mu\text{m}$ the crack and Li filament propagate in unison and the crack profiles are similar in both cases, but for $a > 50 \mu\text{m}$ the crack openings are larger for $R_{\text{Tip}} = 22 \Omega\text{cm}$ compared to those for $R_{\text{Tip}} = 0$. These larger openings induce larger crack flank tractions (compared Figure 5c and 7c). The larger required crack opening take longer to be built-up by the Li^+ fluxes, and this reduces the crack propagation rate.

4.1. Effect of the Filament Tip Resistance

Predictions of the temporal evolution of the crack length a and Li filament length ζ are included in Figure 8a for three values of the filament tip resistance R_{Tip} and an imposed current density $i_{\infty} = 1 \text{ mA cm}^{-2}$. As discussed above, the crack and Li filament propagate in unison for $R_{\text{Tip}} = 0$. However, for the higher values of R_{Tip} not only does the crack tip propagate more slowly but the divergence between the temporal evolution of a and of ζ also increases with increasing R_{Tip} . An immediate consequence is that the time to crack the electrolyte and the time at which the cell shorts will differ at the higher values of R_{Tip} . This is clearly observed in refs. [28,29], where X-ray imaging shows that the electrolyte has cracked but the cell has not shorted at the time of complete fracture of the electrolyte.

To quantify this difference, we define two failure times: 1) t_{crack} for the cracking of the electrolyte, i.e., the time when $a = L$ and 2) the shorting time t_{short} when $\zeta = L$. Note that for time $t > t_{\text{crack}}$ the electrolyte has fractured with tractions $T_n = 0$ on the crack flanks and the solution of the subsequent filament growth problem is a pure electrochemical solution with no mechanical coupling. Predictions of t_{crack} and t_{short} are included in Figure 8b as a function of the imposed current density i_{∞} for $R_{\text{Tip}} = 0$ and $R_{\text{Tip}} = 22 \Omega\text{cm}$. For $R_{\text{Tip}} = 0$, $t_{\text{crack}} = t_{\text{short}}$ so that cracking of the electrolyte is synonymous with shorting of the cell in line with observations for LLZO. On the other hand,

shorting occurs significantly after cracking of the electrolyte in the $R_{\text{Tip}} = 22 \Omega\text{cm}$ case and this is qualitatively consistent with observations for sulfide electrolytes. We thus argue that the differences of cracking and shorting times between LLZO and sulfide electrolytes are related to the fact that excess electrons accumulate on LLZO surfaces but not sulfides. This is parameterised via R_{Tip} in our analysis. In all cases, the cracking and shorting times decrease with increasing i_{∞} as the flux of Li into the crack increases as i_{∞} increases. However, for the sulphide electrolytes the tip resistance R_{Tip} also strongly influences the growth rate of the Li filaments and cracks: the growth rate of both Li filaments and cracks decreases with increasing R_{Tip} for a given i_{∞} .

5. Concluding Remarks

A variational principle for modeling the ingress of Li into solid electrolytes has been developed by making use of Onsager formalism. The Onsager principle^[35,36] allows us to couple together the elastic deformation and cracking of the electrolyte, the electrochemical driving forces in the cell, and the ion transport dissipative processes in the electrolyte bulk and across the electrolyte/electrode and electrolyte/crack interfaces. The kinetics of crack/Li filament propagation along with the shapes of the crack and Li filament are natural outcomes of the solution to the variational problem.

Unlike liquid electrolytes, in solid electrolytes, the elasticity of the solid implies that the crack cannot assume arbitrary shapes if the tractions along the Li filament/crack interface are to remain compressive. Consequently, the mismatch between the time-integrated flux of Li^+ ions into the crack and elastic opening of the crack can result in sparse filling of the cracks with Li, while the resistance to the ability of Li^+ ions to acquire electrons at the Li filament tip implies that the crack can propagate ahead of the Li filament in some cases. The predictions are not only in good qualitative agreement with X-ray CT observations of the cracking of LLZO and LPS electrolytes but are also in excellent quantitative agreement with measured crack velocities.

The framework provides a comprehensive understanding of the kinetics of cracking and Li filament propagation in solid electrolytes. It shows that the mismatch between the elastic crack opening and the flux of Li⁺ ions into the cracks is a maximum near the mouth of the crack at the interface with the plating electrode. Direct X-ray CT observations to measure the extent of filling of cracks as a function of position within the electrolyte have not been reported to date. Such observations are desirable and will serve to further test the fidelity of the modeling framework introduced here.

Supporting Information

Supporting Information is available from the Wiley Online Library or from the author.

Acknowledgements

The authors are grateful for helpful discussions with Professors Peter Bruce and Clare Grey. N.A.F., P.R.S., and S.H. acknowledge support by the Faraday Institution (Solbat, grant no. FIRG007). P.R.S. acknowledges support of The Royal Academy of Engineering (grant no. CIET1718/59).

Conflict of Interest

The authors declare no conflict of interest.

Data Availability Statement

The data that support the findings of this study are available from the corresponding author upon reasonable request.

Keywords

ceramic separators, lithium dendrites, solid-state batteries, variational principles

Received: January 17, 2023

Revised: March 15, 2023

Published online:

- [1] N. Kamaya, K. Homma, Y. Yamakawa, M. Hirayama, R. Kanno, M. Yonemura, T. Kamiyama, Y. Kato, S. Hema, K. Kawamoto, A. Mitsui, *Nat. Mater.* **2011**, *10*, 682.
- [2] P. G. Bruce, S. A. Freunberger, L. J. Hardwick, J.-M. Tarascon, *Nat. Mater.* **2012**, *11*, 19.
- [3] K. Takada, *Acta Mater.* **2013**, *61*, 759.
- [4] K. B. Hatzell, X. Chelsea Chen, C. L. Cobb, N. P. Dasgupta, M. B. Dixit, L. E. Marbella, M. T. McDowell, P. P. Mukherjee, A. Verma, V. Viswanathan, A. S. Westover, *ACS Energy Lett.* **2020**, *5*, 922.
- [5] L. Porz, T. Swamy, B. W. Sheldon, D. Rettenwander, T. Frömling, H. L. Thaman, S. Berendts, R. Uecker, W. C. Carter, Y.-M. Chiang, *Adv. Energy Mater.* **2017**, *7*, 1701003.
- [6] F. Flatscher, M. Philipp, S. Ganschow, H. M. R. Wilkening, D. Rettenwander, *J. Mater. Chem. A* **2020**, *8*, 15782.
- [7] L. Cheng, W. Chen, M. Kunz, K. Persson, N. Tamura, G. Chen, M. Doeff, *ACS Appl. Mater. Interfaces* **2015**, *7*, 2073.
- [8] A. Sharafi, H. M. Meyer, J. Nanda, J. Wolfenstine, J. Sakamoto, *J. Power Sources* **2016**, *302*, 135.
- [9] A. Sharafi, C. G. Haslam, R. D. Kerns, J. Wolfenstine, J. Sakamoto, *J. Mater. Chem. A* **2017**, *5*, 21491.
- [10] E. Kazyak, R. Garcia-Mendez, W. S. LePage, A. Sharafi, A. L. Davis, A. J. Sanchez, K.-H. Chen, C. Haslam, J. Sakamoto, N. P. Dasgupta, *Matter* **2020**, *2*, 1025.
- [11] A. Sharafi, E. Kazyak, A. L. Davis, S. Yu, T. Thompson, D. J. Siegel, N. P. Dasgupta, J. Sakamoto, *Chem. Mater.* **2017**, *29*, 7961.
- [12] C.-L. Tsai, V. Roddatis, C. Vinod Chandran, Q. Ma, S. Uhlenbruck, M. Bram, P. Heitjans, O. Guillon, *ACS Appl. Mater. Interfaces* **2016**, *8*, 10617.
- [13] J. Kasemchainan, S. Zekoll, D. Spencer Jolly, Z. Ning, G. O. Hartley, J. Marrow, P. G. Bruce, *Nat. Mater.* **2019**, *18*, 1105.
- [14] T. Deng, X. Ji, Y. Zhao, L. Cao, S. Li, S. Hwang, C. Luo, P. Wang, H. Jia, X. Fan, X. Lu, *Adv. Mater.* **2020**, *32*, 2000030.
- [15] M. B. Dixit, M. Regala, F. Shen, X. Xiao, K. B. Hatzell, *ACS Appl. Mater. Interfaces* **2018**, *11*, 2022.
- [16] K. J. Harry, D. T. Hallinan, D. Y. Parkinson, A. A. MacDowell, N. P. Balsara, *Nat. Mater.* **2014**, *13*, 69.
- [17] D. Spencer Jolly, Z. Ning, J. E. Darnbrough, J. Kasemchainan, G. O. Hartley, P. Adamson, D. E. J. Armstrong, J. Marrow, P. G. Bruce, *ACS Appl. Mater. Interfaces* **2019**, *12*, 678.
- [18] L. Barroso-Luque, Q. Tu, G. Ceder, *J. Electrochem. Soc.* **2020**, *167*, 020534.
- [19] P. Barai, A. T. Ngo, B. Narayanan, K. Higa, L. A. Curtiss, V. Srinivasan, *J. Electrochem. Soc.* **2020**, *167*, 100537.
- [20] P. Barai, K. Higa, V. Srinivasan, *J. Electrochem. Soc.* **2018**, *165*, A2654.
- [21] M. Klinsmann, F. E. Hildebrand, M. Ganser, R. M. McMeeking, *J. Power Sources* **2019**, *442*, 227226.
- [22] F. Yang, *Phys. Chem. Chem. Phys.* **2020**, *22*, 13737.
- [23] R. D. Armstrong, T. Dickinson, J. Turner, *Electrochim. Acta* **1974**, *19*, 187.
- [24] G. Bucci, J. Christensen, *J. Power Sources* **2019**, *441*, 227186.
- [25] H. Haftbaradaran, S. Esmizadeh, A. Salvadori, *Int. J. Solids Struct.* **2022**, *254*, 111852.
- [26] S. S. Shishvan, N. A. Fleck, R. M. McMeeking, V. S. Deshpande, *J. Power Sources* **2020**, *456*, 227989.
- [27] S. S. Shishvan, N. A. Fleck, R. M. McMeeking, V. S. Deshpande, *Acta Mater.* **2020**, *196*, 444.
- [28] Z. Ning, D. Spencer Jolly, G. Li, R. De Meyere, S. D. Pu, Y. Chen, J. Kasemchainan, J. Ihli, C. Gong, B. Liu, D. L. R. Melvin, A. Bonnin, O. Magdysyuk, P. Adamson, G. O. Hartley, C. W. Monroe, T. J. Marrow, P. G. Bruce, *Nat. Mater.* **2021**, *20*, 1121.
- [29] S. Hao, S. R. Daemi, T. M. Heenan, W. Du, C. Tan, M. Storm, C. Rau, D. J. Brett, P. R. Shearing, *Nano Energy* **2021**, *82*, 105744.
- [30] S. Hao, J. J. Bailey, F. Iacoviello, J. Bu, P. S. Grant, D. J. Brett, P. R. Shearing, *Adv. Funct. Mater.* **2021**, *31*, 2007564.
- [31] C. D. Fincher, D. Ojeda, Y. Zhang, G. M. Pharr, M. Pharr, *Acta Mater.* **2020**, *186*, 215.
- [32] C. Xu, Z. Ahmad, A. Aryanfar, V. Viswanathan, J. R. Greer, *Proc. Natl. Acad. Sci. U.S.A* **2017**, *114*, 57.
- [33] L. Zhang, T. Yang, C. Du, Q. Liu, Y. Tang, J. Zhao, B. Wang, T. Chen, Y. Sun, P. Jia, H. Li, L. Geng, J. Chen, H. Ye, Z. Wang, Y. Li, H. Sun, X. Li, Q. Dai, Y. Tang, Q. Peng, T. Shen, S. Zhang, T. Zhu, J. Huang, *Nat. Nanotechnol.* **2020**, *15*, 94.
- [34] C. D. Fincher, C. E. Athanasiou, C. Gilgenbach, M. Wang, B. W. Sheldon, W. Craig Carter, Y.-M. Chiang, *Joule* **2022**, *6*, 2794.
- [35] L. Onsager, *Phys. Rev.* **1931**, *37*, 405.
- [36] L. Onsager, *Phys. Rev.* **1931**, *38*, 2265.
- [37] A. A. Griffith, *Phil. Trans. R. Soc. London A* **1921**, *221*, 163.

- [38] H. Tada, P. Paris, G. Irwin, *The Stress Analysis of Cracks Handbook*, ASME Press, New York, NY **2000**.
- [39] H.-K. Tian, Z. Liu, Y. Ji, L.-Q. Chen, Y. Qi, *Chem. Mater.* **2019**, *31*, 7351.
- [40] A. Sharafi, C. G. Haslam, R. D. Kerns, J. Wolfenstine, J. Sakamoto, *J. Mater. Chem. A* **2017**, *5*, 21491.
- [41] K. N. Wood, E. Kazyak, A. F. Chadwick, K.-H. Chen, J.-G. Zhang, K. Thornton, N. P. Dasgupta, *ACS Cent. Sci.* **2016**, *2*, 790.
- [42] M. Wang, J. Sakamoto, *J. Power Sources* **2018**, *377*, 7.
- [43] J. E. Ni, E. D. Case, J. S. Sakamoto, E. Rangasamy, J. B. Wolfenstine, *J. Mater. Sci.* **2012**, *47*, 7978.